



30 for observing dynamic behavior of the CSWs.

31

32 **Keywords:** Continental shelf wave; Arrested topographic wave; Cross-shelf SLA
33 structure; South China Sea

34

35 **1 Introduction**

36 The South China Sea (SCS) is the largest semi-enclosed marginal sea of the west
37 Pacific Ocean. It communicates with the Pacific Ocean by the Luzon Strait in the east
38 and the East China Sea (ECS) by the Taiwan Strait in the northeast. In the south, the
39 SCS is jointed to the Indonesian Seas by the Karimata Strait. The SCS is characterized
40 by wide continental shelves, occupying 48% of the total area (Zheng et al., 2006). A
41 deep basin in the central area occupies 16% of the entire region.

42 Sea level variation is a valuable indicator of upper ocean processes. Under the
43 background of global warming, the sea level variation in such a large semi-enclosed
44 marginal sea has been investigated by previous investigators. Ho et al. (2000) found
45 seasonal sea level variability in the SCS using data from a satellite altimeter. Kajikawa
46 and Yasunari (2005) investigated the interannual variability of the intra-seasonal
47 variation over the SCS. Fang et al. (2006) analyzed low sea level along the eastern
48 boundary of the SCS. Rong et al. (2007) investigated the relationship between ENSO
49 (El Niño and Southern Oscillation) and interannual variability of sea level in the SCS.
50 Zhuang et al. (2010) found strong intra-seasonal variability in the northern SCS. In
51 addition, the sea level variations are influenced by thermodynamic processes, e.g.,
52 eddies and thermal change of upper layer of the SCS (Cheng and Qi, 2007; Xie et al.,
53 2018; Zheng et al., 2014).

54 The coastal sea-level variations are particularly important, as the continental shelf
55 occupies about half area of the SCS. Meanwhile, the upper layer thermal changes
56 significantly influence the sea level variations (Cheng and Qi, 2007). Wang et al. (2017)
57 found that seasonal level anomalies are closely related to ENSO events (Wang et al.,
58 2022). Using sea surface height (SSH) data from a satellite altimeters, Xu et al. (2016)
59 found that sea level variations in the coastal area of the SCS are still strongly influenced

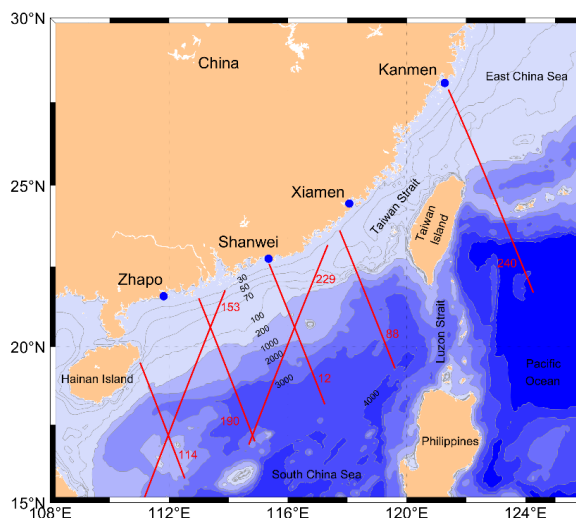


60 by the coastal current system in summer and winter. Seasonal circulation is mainly
61 driven by the monsoon wind stress (Gan et al., 2006). Lin et al. (2021) applied the
62 arrested topographic waves (ATWs) model to the coastal mean dynamic topography
63 along the ECS and the SCS. It suggests that the mean dynamic topography is a
64 counterbalance of contributions from the along-shelf wind and well predicted by the
65 ATW model. Therefore, the monsoon winds are a control factor for the sea level
66 variation.

67 In the synoptic time scale (~week), the sea level variations in the coastal area
68 induced by storms act as continental shelf waves (CSWs) in the SCS. The CSWs are
69 typical sub-inertial motions resulting from conserving potential vorticity over the shelf.
70 The CSW events reported by previous investigators lasted from 2 days to 2 weeks (Chen
71 and Su, 1987; Li et al., 2015; Li et al., 2021; Zheng et al., 2015). The phase speed of
72 CSWs depends on the bottom topography, ranging from 5 to 20 m s⁻¹ (Li et al., 2015;
73 Li et al., 2016; Shen et al., 2021).

74 The sea level variations in the SCS are well depicted by these previous studies.
75 However, two issues should be improved. The first is that the primary data are usually
76 obtained from the tide-gauge stations along the coastline. The data have high accuracies,
77 but represent the sea level at the coasts only. Thus, satellite-altimeter-observed the sea
78 level variation are often used to fill the data gaps in between the tide-gauge stations and
79 on the continental shelf. The second issue is that the repeated period of the satellite
80 altimeter is 9.9 d, which is challenging to investigate the sea level variations with
81 periods shorter than 10 d. Previous studies used the along-track sea level anomaly (SLA)
82 from satellite altimeters to describe CSW (Chen et al., 2014; Li et al., 2016). However,
83 the satellite altimeter with the sparse tracks (as shown in Fig. 1) could only capture the
84 cross-structure of CSW with one or two snapshot of one CSW.

85



86

87 **Fig. 1.** Study area. Blue dots represent locations of tide-gauge stations Kanmen,
88 Xiamen, Shanwei, and Zhapo. Red lines represent segments of ground tracks 12, 88,
89 114, 153, 190, 229, and 240 for altimeter satellites over the continental shelf. Tracks 12,
90 88, 114, and 240 are almost perpendicular to the coastline. Isobaths are in m.

91

92 This study aims to investigate the cross-shelf structures of sea level over the
93 continental shelf. As the repeated period of the satellite altimeters, 9.9 d, is comparable
94 with that of CSWs in the northern SCS, the statistical characteristics of the along-track
95 SLA are applied to show the cross-shelf structure of CSWs using a long-term data set
96 from 1993 to 2020. To figure out the cross-shelf structures of ATWs is another goal.

97 The rest of the paper is organized as follows: Section 2 describes the observed data
98 and the analysis methods. Section 3 presents the characteristics of the signals derived
99 from the tide-gauge data and along-track SLA. Section 4 presents the theory of CSW
100 and ATW. Section 5 discusses the CSWs detected from tide-gauge data and the cross-
101 shelf structure of sea level over the continental shelf. Section 6 gives summaries.

102

103 **2 Data and methodology**

104 **2.1 Along-track sea level anomaly data**

105 Satellite altimeter along-track SLA data are produced and distributed by the
106 Archiving, Validation, and Interpretation of Satellite Oceanographic Data (AVISO),



107 Centre National d'Etudes Spatiales (CNES) of France. The data from 1993 to 2020 are
108 derived from TOPEX/Poseidon, Jason-1, Jason-2, and Jason-3 measurements. The
109 satellite repetition period is 9.9 d, and the temporal resolution of the along-track data is
110 1 Hz. The along-track SLA is calculated by subtracting the twenty-year mean from the
111 SSH measured by the satellite altimeters. The ground tracks in the study area, 12, 88,
112 114, 153, 229, and 240, are shown in Fig. 1.

113

114 2.2 Sea level anomaly from tide-gauge

115 The tide-gauge data at stations Kanmen, Xiamen, Shanwei, Hongkong and Zhapo
116 (as shown in Fig. 1) are obtained from the Global Sea Level Observing System
117 (GLOSS). The data cover a period from 1993 to 1997, with a temporal resolution of 1
118 h. De-tided sea level anomaly (DSL_A) is calculated by removing tidal signals using a
119 Matlab toolbox (Pawlowicz et al., 2002).

120 The monthly sea level means at stations Xiamen, Shanwei, and Zhapo are obtained
121 from the Permanent Service for Mean Sea Level (PSMSL). Monthly mean data cover
122 periods of 1993-2003, 1993-1994, and 1993-2020 for stations Xiamen, Shanwei, and
123 Zhapo, respectively.

124

125 2.3 Sea surface wind stress

126 Monthly sea surface wind stress is derived from the Copernicus Marine
127 Environment Monitoring Service (CMEMS). The dataset covers a period from 1993 to
128 2020 with a spatial resolution of $0.25^\circ \times 0.25^\circ$. Sea surface wind stress data on the
129 satellite altimeter ground tracks are decomposed into the cross-shelf and along-shelf
130 components. The cross-shelf component is positive seaward and parallel to the satellite
131 altimeter ground tracks (12, 88, 114 and 190). The along-shelf component is positive
132 northward and perpendicular to these satellite altimeter ground tracks.

133

134 2.4 Topographic profile

135 The behavior of continental shelf waves is determined by the topography of the
136 continental shelf and slope, which has been well documented. The topographic profiles



137 along the satellite altimeter ground tracks are extracted from a dataset of ETOPO-2.
138 This study uses one-dimensional linear piecewise functions to fit the topographic
139 profiles along the satellite altimeter ground tracks. The width of the continental shelf,
140 depths of shelf break and deep basin along the tracks are listed in Table 1. The
141 continental shelf break is extracted as the location of maximum change in the gradient
142 of continental slope.

143

144 Table 1. The width of the continental shelf, depths of shelf break and deep basin along
145 the satellite ground tracks.

Track number	l (km)	H_1 (m)	H_2 (m)
12	200	-300	-3800
88	178	-200	-2500
114	123	-200	-1800
153	259	-110	-1600
190	247	-255	-3500
229	244	-225	-3500
240	273	-250	-5000

146

147 2.5 Wavelet analysis

148 The wavelet transform (WT) is an effective method for analyzing nonstationary
149 time series (Torrence and Compo, 1998). The transform for time series, x_n , with the
150 scaled and normalized wavelet

$$151 \quad W_n^X(s) = \sqrt{\delta t/s} \sum_{n'=1}^N x_{n'} \psi[(n' - n)\delta t/s] \quad (1)$$

152 where s is the wavelet scale, δt is uniform time spacing, ψ is the Morlet wavelet, $\psi(\eta) =$
153 $\pi^{-1/4} e^{-i\omega_0\eta} e^{-\frac{1}{2}\eta^2}$, and $n = 0, 1, \dots, N - 1$ (N is the data number). The covariance of
154 two-time series X and Y , $|W_n^{XY}(s)| = |W_n^X(s)W_n^{Y*}(s)|$, is used to analyze the
155 relationship in cross wavelet transform (XWT):

$$156 \quad vZ_v^{-1}(p/2)|W_n^X(s)W_n^{Y*}(s)| \leq |\omega_n^X(s)\omega_n^Y(s)| \leq vZ_v^{-1}(1 - p/2)|W_n^X(s)W_n^{Y*}(s)| \quad (2)$$

157 where $Z_v(p)$ is the confidence level associated with the significance p , * denotes
158 complex conjugation. The phase difference between two time series can be expressed



159 as a phase angle a_m (Grinsted et al., 2004):

160
$$a_m = \arg(X, Y) \text{ with } X = \sum_{i=1}^n \cos a_i \text{ and } Y = \sum_{i=1}^n \sin a_i \quad (3)$$

161 where a_i is the phase angle of signals.

162

163 **3 Signals in sea level anomaly**

164 **3.1 Tide-gauge data**

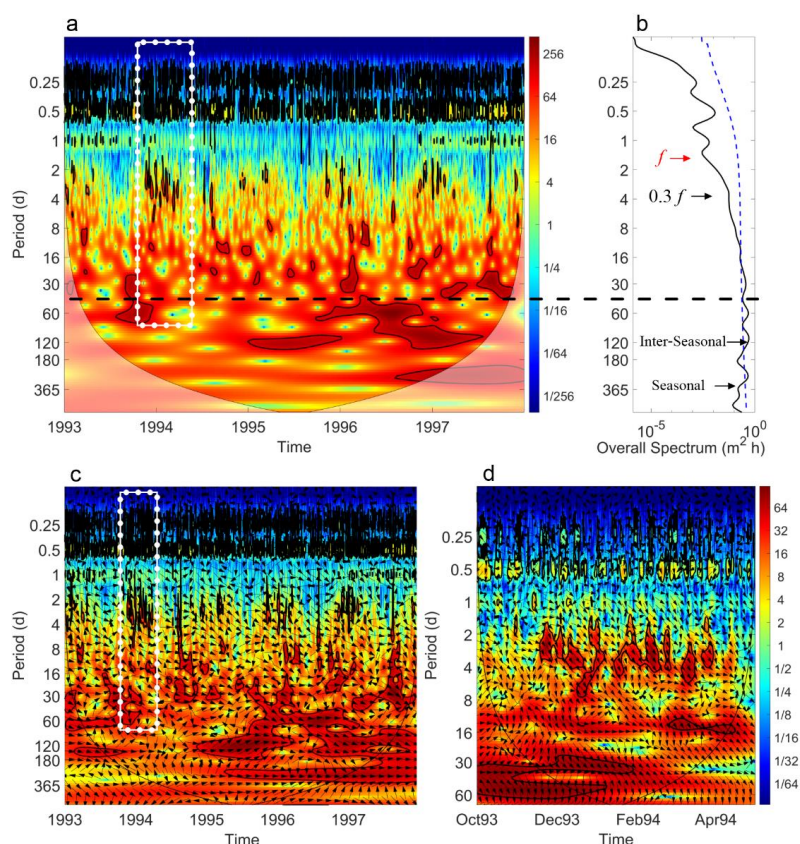
165 Fig. 2 shows the WT of SLA at station Xiamen from 1993 to 1997. One can see
166 abundant signals with periods from several days to one year in Figs.2a-b. A dozen
167 signals with periods from several days to about one month could be seen from the WT
168 of SLA every year. The duration of these signals, with a period of several days, is about
169 ten days. Moreover, the signals with a period of about one month sustain for about three
170 months. Even if significance level against red noise is less than 5%, the power is
171 universal and continuous in the period bands of 10-60 d. The main reason is that these
172 signals are not so significant compared with the signals with large amplitude. The
173 wavelet analysis also exhibits a significant inter-seasonal and seasonal variation of SLA.
174 The characteristics of the signals at stations Kanmen, Shanwei, and Zhapo are almost
175 the same (not shown here). Therefore, the variation of SLA along the northern SCS
176 coast is universal.

177 Figs. 2c-d show the XWT of SLA between stations Kanmen and Xiamen. One can
178 see that the period band and the occurrence time of the significant cross wavelet power
179 are consistent with that in Fig. 2a. The signals with periods shorter and longer than 40
180 d show remarkably different characteristics. In the period band shorter than 40 d, the
181 signals at station Xiamen lag that at station Kamen about 15 h. The propagation phase
182 speed of the sea level signal could be calculated by the lag time of sea level propagation
183 between stations Kanmen and Xiamen. The result is about 9 m s^{-1} , which is very close
184 to that reported by a number of recent studies (Ding et al., 2012; Li et al., 2015; Li et
185 al., 2016; Zhao et al., 2017).

186 In the period band longer than 40 d, the phase of signals between Kanmen and
187 Xiamen is a little complicated. The signal phase with the period of 360 d from 1995 to
188 1997 is almost 0. However, the seasonal signals at station Xiamen lag (lead) that at



189 station Kanmen in winter (summer) about $\pi/4$ - $\pi/2$, implying that the signal propagates
 190 very slowly along the coast. Csanady (1978) concluded that these signals are a kind of
 191 ATWs.
 192



193
 194 **Fig. 2.** Temporal variability of SLA at the coastline. (a) WT of SLA at station Xiamen.
 195 (b) Overall spectrum of SLA at station Xiamen. (c) XWT of SLA between stations
 196 Kanmen and Xiamen. (d) XWT of SLA between stations Kanmen and Xiamen from
 197 October 1993 to April 1994. The thick line is a 5% significance level against red noise,
 198 and the cone of influence (COI) is shown as the thin line. Color codes of power spectra
 199 normalized by variance are in arbitrary units. White dotted rectangles in (a) and (c)
 200 show the temporal domain of (d). The Blue dashed curve in (b) is a 5% significance
 201 level. Arrows in (b) point out the characteristic frequencies of inertial oscillation and
 202 CSWs. The black dashed lines in (a) and (b) represent signal period boundary (40 d).
 203 The arrows in (c) and (d) show the relative phase relationship between SLA at Kanmen
 204 and Xiamen with in-phase (anti-phase, leading, and lagging) pointing right (left,
 205 and up).



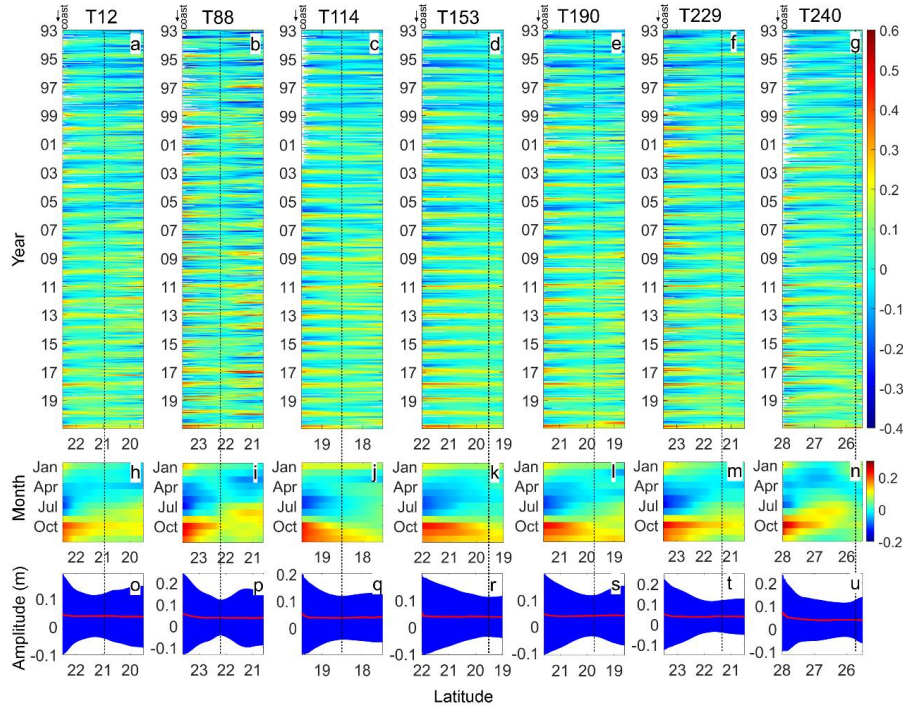
206

207 3.2 Along-track SLA

208 Fig. 3 shows the latitude distribution of along-track SLA over the northern
209 continental shelf of the SCS from 1993 to 2020. One can see the clear annual signals
210 near the coast in Figs. 3a-g. Signals with periods shorter than one year could also be
211 seen. As shown in Figs. 3h-n, a clear seasonal cycle is discernable from the
212 climatological monthly mean of along-track SLA. One can see that lower (higher) sea
213 levels over the shelf exist from March to August (September to February). The trough
214 (~ -0.2 m) and peak (~ 0.24 m) of sea level near the coast occur in July and October,
215 respectively. The 28-year mean value of along-track SLA is about 0.04 m, as shown in
216 Figs. 3o-u.

217 Moreover, the standard deviations (STD) of along-track SLA from 1993 to 2020
218 (blue shadow in Figs. 3o-u) show a bell-mouth-like structure over the shelf. The
219 amplitudes of along-track SLA reach the maxima near the coast. The minimum variance
220 exists near the shelf edge. The cross-shelf structure of SLA indicates that sea-level
221 signals depend on the shelf depth.

222



223

224 **Fig. 3.** (a-g) Latitudinal distribution of along-track SLA over the northern continental
 225 shelf of the SCS from 1993 to 2020 for tracks 12, 88, 114,153, 190, 229, and 240,
 226 respectively. (h-n) Climatological monthly mean of along-track SLAs for Tracks 12, 88,
 227 114,153, 190, 229, and 240. (o-u) Mean (red curves) and standard deviation (blue
 228 shadow) of along-track SLA from 1993 to 2020 for tracks 12, 88, 114,153, 190, 229,
 229 and 240. Track numbers are shown on the tops of panels. Vertical dashed lines represent
 230 shelf break positions along the tracks, i.e., H1, listed in Table 1. The coastline position
 231 is marked by an arrow on top left of each panel.

232

233 4 Dynamic analysis

234 4.1 Momentum equation for CSWs

235 The linearized shallow-water equations governing a barotropic ocean on a rotating
 236 earth are

$$237 \quad \frac{\partial u}{\partial t} - fv = -g \frac{\partial \eta}{\partial x} + \frac{\tau_s^x - \tau_b^x}{\rho H} \quad (4a)$$

$$238 \quad \frac{\partial v}{\partial t} + fu = -g \frac{\partial \eta}{\partial y} + \frac{\tau_s^y - \tau_b^y}{\rho H} \quad (4b)$$

$$239 \quad \frac{\partial \eta}{\partial t} + \frac{\partial(uH)}{\partial x} + \frac{\partial(vH)}{\partial y} = 0 \quad (4c)$$

240 where cross-shelf and along-shelf velocities (u, v) are depth-averaged in cross-shelf and



241 along-shelf coordinates (x, y) . η is the sea surface height. The Coriolis parameter is f .
 242 The bathymetry $H=H(x)$ is assumed to be a function of the cross-shelf variable, x only.
 243 τ_s and τ_b the surface and bottom stresses. g, ρ are the gravitational acceleration and
 244 the water density.

245 The scales of the along-shelf length of CSW ($L = 2\pi/k \approx 2 \times 10^3$ km), and
 246 cross-shelf length ($l \approx 200$ km) are subject to the long-wave assumptions ($l/L \ll 1$),
 247 i.e., $\partial u/\partial t = 0$ (Li et al., 2016; Schulz et al., 2011). Under this approximation, Eqs.
 248 (4a) and (4b) become

$$249 \quad v = \frac{g}{f} \frac{\partial \eta}{\partial x} - \frac{\tau_s^x - \tau_b^x}{f \rho H} \quad (5a)$$

$$250 \quad u = -\frac{g}{f} \frac{\partial \eta}{\partial y} - \frac{\partial}{\partial t} \left(\frac{g}{f^2} \frac{\partial \eta}{\partial x} - \frac{\tau_s^x - \tau_b^x}{f^2 \rho H} \right) + \frac{\tau_s^y - \tau_b^y}{f \rho H} \quad (5b)$$

251 Substitute Eqs. (5a) and (5b) into Eq. (4c), we obtain the equation governing
 252 SSH of CSWs

$$253 \quad \frac{\partial}{\partial t} \left(\eta - \frac{gH}{f^2} \frac{\partial^2 \eta}{\partial x^2} - \frac{g}{f^2} \frac{\partial \eta}{\partial x} \frac{dH}{dx} \right) - \frac{g}{f} \frac{\partial \eta}{\partial y} \frac{dH}{dx} + \frac{\partial}{\partial x} \left(\frac{\tau_s^y - \tau_b^y}{f \rho} \right) + \frac{\partial^2}{\partial t \partial x} \left(\frac{\tau_s^x - \tau_b^x}{f^2 \rho} \right) - H \frac{\partial}{\partial y} \left(\frac{\tau_s^x - \tau_b^x}{f \rho H} \right) = 0 \quad (6)$$

255 Assume that CSWs are forced by along-shelf wind stress, i.e., $(\tau_s^x, \tau_s^y) = (0, \tau_s^y)$.
 256 The bottom friction is neglected to simplify the calculation in Eq. (6). Therefore, the
 257 equation governing the SSH of CSWs becomes

$$258 \quad \frac{\partial}{\partial t} \left(\eta - \frac{gH}{f^2} \frac{\partial^2 \eta}{\partial x^2} - \frac{g}{f^2} \frac{\partial \eta}{\partial x} \frac{dH}{dx} \right) - \frac{g}{f} \frac{\partial \eta}{\partial y} \frac{dH}{dx} + \frac{\partial}{\partial x} \left(\frac{\tau_s^y}{f \rho} \right) = 0 \quad (7)$$

259 The change in the SSH of CSWs is balanced by the variation of along-shelf wind
 260 stress in cross-shelf direction. Assume a periodic along-shelf wind stress, $\tau_s^y =$
 261 $\tau_0 \exp[i(\alpha y + \omega t)]$ (where α is wavenumber of wind stress, and $\tau_0 =$ constant). Eq.
 262 (7) becomes

$$263 \quad \frac{\partial}{\partial t} \left(\eta - \frac{gH}{f^2} \frac{\partial^2 \eta}{\partial x^2} - \frac{g}{f^2} \frac{\partial \eta}{\partial x} \frac{dH}{dx} \right) - \frac{g}{f} \frac{\partial \eta}{\partial y} \frac{dH}{dx} = 0 \quad (8)$$

264 which means that the change in SSH is independent of along-shelf wind stress.

265 The assumption of a wave solution

$$266 \quad \eta = \phi(x) \exp[i(ky + \omega t)] \quad (9)$$

267 yields an equation for $\phi(x)$,



268
$$H \frac{d^2 \phi}{dx^2} + \frac{dH}{dx} \frac{d\phi}{dx} + \left(\frac{fk}{\omega} \frac{dH}{dx} - \frac{f^2}{g} \right) \phi = 0$$
 (10)

269

270 4.1.1 Over the shelf

271 For $0 \leq x \leq l$, $H = H_1 x/l$, the equation for $\phi(x)$ is

272
$$x \frac{d^2 \phi}{dx^2} + \frac{d\phi}{dx} + \left(\frac{fk}{\omega} - \frac{f^2 l}{g H_1} \right) \phi = 0$$
 (11)

273 The solution to Eq. (11) is expressed as the sum of the first and second kinds of
274 Bessel functions (Schulz et al., 2011)

275
$$\phi(x) = a J_0 \left(2 \left(\frac{fk}{\omega} - \frac{f^2 l}{g H_1} \right)^{\frac{1}{2}} x^{\frac{1}{2}} \right) + b Y_0 \left(2 \left(\frac{fk}{\omega} - \frac{f^2 l}{g H_1} \right)^{\frac{1}{2}} x^{\frac{1}{2}} \right)$$
 (12)

276 where a is arbitrary constant. As the solution for $\phi(x)$ is finite, therefore

277
$$\phi(x) = a J_0 \left(2 \left(\frac{fk}{\omega} - \frac{f^2 l}{g H_1} \right)^{\frac{1}{2}} x^{\frac{1}{2}} \right)$$
 (13)

278

279 4.1.2 In the deep basin

280 For $l < x$, $H = H_2$, the equation for $\phi(x)$ is

281
$$\frac{d^2 \phi}{dx^2} - \frac{f^2}{g H_2} \phi = 0$$
 (14)

282 The solution is

283
$$\phi(x) = A \exp \left(-\frac{fl}{\sqrt{g H_2}} \left(\frac{x}{l} - 1 \right) \right) + B \exp \left(\frac{fl}{\sqrt{g H_2}} \left(\frac{x}{l} - 1 \right) \right)$$
 (15)

284 As the solution for $\phi(x)$ is also finite in the deep basin, i.e.,

285
$$\phi(x) = A \exp \left(-\frac{fl}{\sqrt{g H_2}} \left(\frac{x}{l} - 1 \right) \right)$$
 (16)

286 where A is arbitrary constant.

287

288 4.1.3 Dispersion relation

289 As the fluid is continuous at the edge of continental shelf, therefore

290
$$H_1 \cdot u|_{x \rightarrow l^-} = H_2 \cdot u|_{x \rightarrow l^+}$$
 (17a)



291
$$aJ_0 \left(2 \left(\frac{fkl}{\omega} - \frac{f^2 l^2}{gH_1} \right)^{\frac{1}{2}} \right) = A \quad (17b)$$

292 From Eq. (17a), we have

293
$$H_1 \cdot a \left(kJ_0 + \frac{\omega}{f} \left(\frac{fk}{\omega l} - \frac{f^2}{gH_1} \right)^{\frac{1}{2}} J_0' \right) = H_2 \cdot A \left(k - \frac{\omega}{\sqrt{gH_2}} \right) \quad (18)$$

294 where J_0' is the derivation of the zero-order of the first kind Bessel function,

295
$$J_0'(x) = -\frac{x}{2} (J_0(x) + J_2(x)) \quad (19)$$

296 where J_2 is the second order of J_0 .

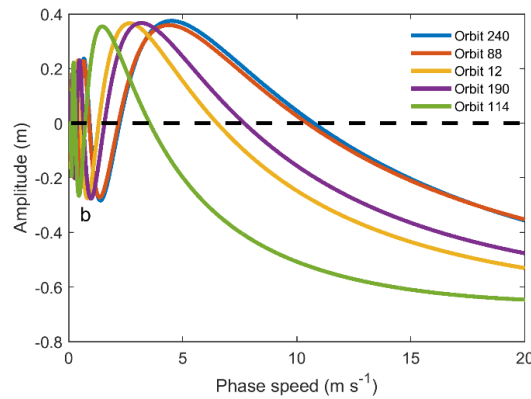
297 Substituting Eq. (19) into Eq. (18) yields a dispersion relation for CSWs

298
$$\left(\frac{cfl}{gH_2} - 1 + \frac{c}{(gH_2)^{\frac{1}{2}}} \right) J_0 - \left(\frac{H_1}{H_2} - \frac{cfl}{gH_2} \right) J_2 = 0 \quad (20)$$

299 where $c (= \frac{\omega}{k})$ is the phase speed of CSWs. We solve Eq. (20) using the zero-finding

300 function in MATLAB.

301



302

303 **Fig. 4.** Solution of phase speed for CSWs from Eq. (20). The zero-crossing values
 304 represent the phase speed of CSWs for different modes. Colorful curves are amplitude
 305 of zero-order of the first kind Bessel function in different modes for the idealized depth
 306 profile of tracks 12, 88, 114, 190, and 240, respectively.

307

308 4.1.4 Cross-shelf structure

309 With Eqs. (13), (16) and (17b), the wave solution of SSH, i.e., Eq. (6), is



$$\eta = \begin{cases} \sum_{i=1}^{\infty} a_i \cdot J_0 \left(2 \left(\frac{fk_i}{\omega_i} - \frac{f^2 l}{gH_1} \right)^{\frac{1}{2}} x^{\frac{1}{2}} \right) \exp[i(k_i y + \omega_i t)] & x \leq l \\ \sum_{i=1}^{\infty} a_i \cdot J_0 \left(2 \left(\frac{fk_i l}{\omega_i} - \frac{f^2 l^2}{gH_1} \right)^{\frac{1}{2}} \right) \exp \left(-\frac{fl}{\sqrt{gH_2}} \left(\frac{x}{l} - 1 \right) \right) \exp[i(k_i y + \omega_i t)] & x > l \end{cases} \quad (21)$$

where $\exp[i(ky + \omega t)]$ is the waveform propagating along the shelf. $a_i \cdot J_0$ is the cross-shelf structure of the waveform for mode i over the shelf.

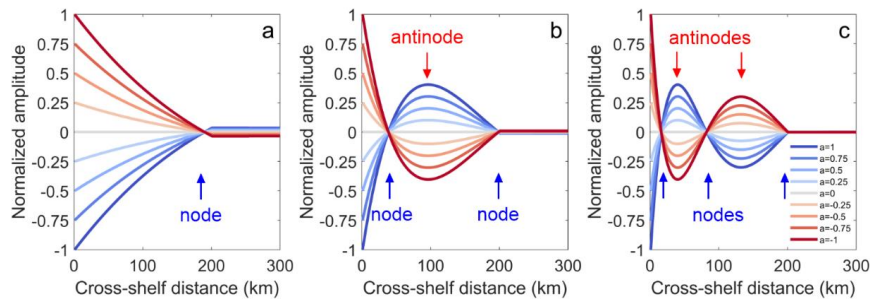
In the cross-shelf direction, the SSH becomes

$$\eta = \begin{cases} \sum_{i=1}^{\infty} \eta_{0i}(t) \cdot J_0 \left(2 \left(\frac{fk_i}{\omega_i} - \frac{f^2 l}{gH_1} \right)^{\frac{1}{2}} x^{\frac{1}{2}} \right) & x \leq l \\ \sum_{i=1}^{\infty} \eta_{0i}(t) \cdot J_0 \left(2 \left(\frac{fk_i l}{\omega_i} - \frac{f^2 l^2}{gH_1} \right)^{\frac{1}{2}} \right) \exp \left(-\frac{fl}{\sqrt{gH_2}} \left(\frac{x}{l} - 1 \right) \right) & x > l \end{cases} \quad (22)$$

where $\eta_{0i}(t) (= a_i \exp[i(k_i y + \omega_i t)])$ is time series of SSH at the coastline for mode i .

Fig. 5 shows the SSH evolution over the continental shelf. The SSH Mode 1 looks like a bell mouth, similar to the STD of the along-track SLA over the continental shelf (Figs. 3o-u). For Modes 2 and 3, nodes and antinodes appear over the shelf. Node for Mode 2 appears at 50 km off the coast over the shelf. Nodes for Mode 3 appear at 30 and 90 km off the coast.

323



324

Fig. 5. (a-c) Cross-shelf structure of normalized amplitudes of the first three CSW modes for idealized depth profile of track 12. Gradient color curves represent amplitude evolution over time for CSWs in the cross-shelf direction.

328

329 4.2 Steady situation



330 The governing equations in the steady situation for Eqs. (4a-c) are

$$331 \quad -fv = -g \frac{\partial \eta}{\partial x} \quad (23a)$$

$$332 \quad fu = -g \frac{\partial \eta}{\partial y} + \frac{\tau_s^y - \tau_b^y}{\rho H} \quad (23b)$$

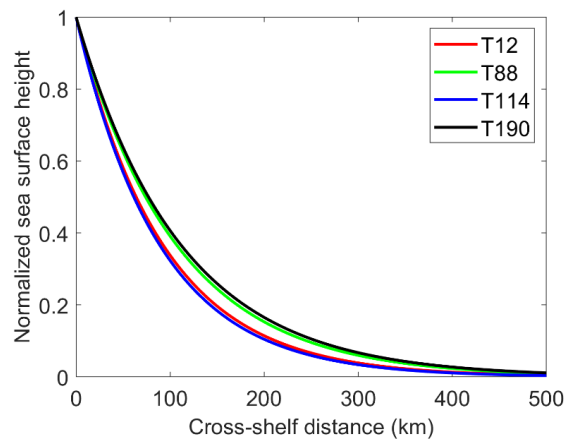
$$333 \quad \frac{\partial(uH)}{\partial x} + \frac{\partial(vH)}{\partial y} = 0 \quad (23c)$$

334 A linear drag is used for the bottom friction, i.e., $\vec{\tau}_b = \rho \lambda \vec{u}$ (Hsueh and Pang, 1989; Lin
335 and Yang, 2011). The SSH Eqs. 23a-c becomes (Csanady, 1978)

$$336 \quad \eta = B \tau_0 e^{-\frac{x}{L}} \sin\left(\alpha y + \frac{x}{L} - \frac{\pi}{4}\right) \quad (21)$$

337 where $L = \sqrt{2\lambda l / \alpha f H_1}$ is the scale width of trapped sea level in the cross-shelf
338 direction, B is an arbitrary constant. A drag coefficient, $\lambda = O(5 \times 10^{-4}) \text{ m s}^{-1}$, is used
339 for the linear bottom friction (Chapman, 1987; Lin and Yang, 2011). The typical
340 magnitude for winter wind stress over the northern continental shelf of the SCS is
341 $O(0.1) \text{ N m}^2$ (Lin and Yang, 2011; Lin et al., 2011). $f = 5 \times 10^{-5} \text{ s}^{-1}$, and $\alpha =$
342 $2\pi/4000 \text{ km}$ evaluated by Lin et al. (2021). The normalized SSH in the cross-shelf
343 direction for tracks 12, 88, 114, and 190 are shown in Fig. 6. One can see that the
344 trapped sea level in the cross-shelf direction decays quickly from 1 at the coastline to
345 ~ 0.2 at the edge of the continental shelf ($\sim 200 \text{ km}$), and 0.1 at a distance of 300 km. As
346 Track 240 is not perpendicular to the coastline, it is beyond the scope.

347



348

349 **Fig. 6.** Normalized SSH in cross-shelf direction for tracks 12, 88, 114, and 190.



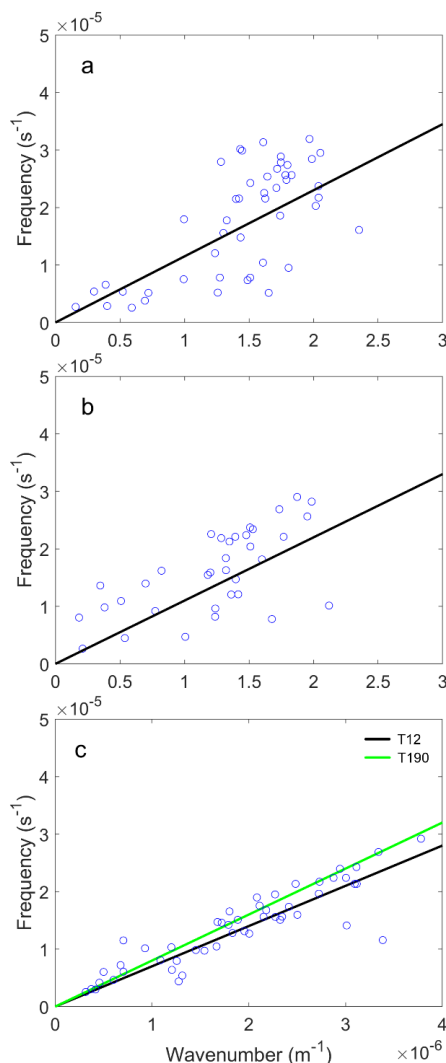
350

351 **5 Discussion**

352 5.1 Propagation of CSWs

353 Fig. 7 compares the data derived from the XWT of SLA with the dispersion
354 relation of CSW. We overlay the dispersion relation curves of CSWs with the results
355 (phase speed, c and period, T , $\lambda = c \cdot T$) from tide-gauge data analysis in Section 3.1.
356 One can see that the data points derived from station pairs are distributed near the
357 dispersion relation of CSWs, implying the signals with the periods shorter than 40 d are
358 the CSWs propagating along the shelf.

359



360

361 **Fig. 7.** Dispersion relation of the lowest mode of CSWs between (a) Kanmen and
 362 Xiamen, (b), Xiamen and Shanwei, as well as (c) Shanwei and Zhapo. The data points
 363 are calculated from the XWT of SLA. The curves are the theoretical dispersion relation
 364 for the mean depth profiles listed in Table 1. Black and green curves in (c) represent the
 365 dispersion relation for the topographic profiles along tracks 12 and 190.

366

367 Figs. 7a and b deal with the signals between Kanmen and Shanwei. We use the
 368 bathymetric profile near Track 240 and 88 of the altimeter satellite to calculate the
 369 dispersion relation curve, respectively. However, since the topography between
 370 Kanmen and Shanwei changes dramatically, the data points lie dispersedly around the



371 curve. The wavenumbers of CSWs range from 0.1 to $2.4 \times 10^{-5} \text{ m}^{-1}$ between stations
372 Kanmen and Shanwei. The CSWs propagate along the coast with a phase speed of 10
373 m s^{-1} .

374 Fig. 7c shows the signals between Shanwei and Zhapo. The data points and the
375 theoretical curves agree quite well. Compared with the topography between Kanmen
376 and Shanwei, the topography changes slightly between stations Shanwei and Zhapo.
377 Thus, we conclude that the signals in tide-gauge data with the periods shorter than 40
378 d are the CSWs propagating along the shelf. The phase speed of CSWs is about 8 m s^{-1}
379 1 in the study area, which is close to that of previous studies (Li et al., 2015; Li et al.,
380 2016; Shen et al., 2021).

381 Previous studies present that the periods of CSWs range from two days to two
382 weeks in the SCS (Chen and Su, 1987; Li, 1993). The period of CSWs upstream, i.e.,
383 in the ECS, is often detected as several days (Ding et al., 2012; Ding et al., 2018; Hsueh
384 and Pang, 1989; Huang et al., 2015; Yin et al., 2014). Hsueh and Romea (1983) found
385 the sea level fluctuations with a period more than 13 d along the West Korean coast.
386 Worldwide, these low-frequency CSWs are common along the coast of Chile and the
387 east coast of the Indian Ocean (Castro and Lee, 1995; Hormazabal et al., 2001; Marshall
388 and Hendon, 2013; Vialard et al., 2009), where the width of the continental shelf is
389 narrow. In this study, we define the CSW with a maximum period of about $30\text{-}40 \text{ d}$. The
390 main reason for the difference is data length we used. The long-time series of DSLA
391 helps analyze the abnormal low-frequency CSWs in the SCS.

392 In addition, we should take care that CSWs in Fig. 7 are mixed with wind-forced
393 CSWs. It is difficult to separate the effect of wind-force and free propagating CSWs
394 clearly. Hsueh and Romea (1983) found that there is clear coupling between surface
395 winds and coastal sea level in the northeast China Sea. Li et al. (2016) found that the
396 propagation time of the wind signals are much shorter than that of CSWs in the NSCS.
397 Even one can see isolated cases which are away from dispersion relationship of CSW
398 in Fig. 7, most of the data points are near the theoretical dispersion relation. Moreover,
399 the stratification in the continental shelf is important for the characteristics of CSW.
400 The sea level variation in this study should present baroclinic and barotropic CSWs in



401 the shelf area together.

402

403 5.2 Trapped cross-shelf structure

404 1) CSWs

405 As the sampling period of the altimeter satellites is about 10 d, the signals with the
406 periods shorter than 20 d could not be distinguished from the along-track SLA based
407 on the Nyquist sampling theorem. Fortunately, the cross-shelf structure of CSWs could
408 be sampled as fragments by repeated satellite observations.

409 In this case, the CSWs with a period less than 40 d were abundant from 1993 to
410 2020 over the northern continental shelf of the SCS, especially in winter (Fig. 2). Even
411 if the significance level is less than 5%, the power is universal and continuous in this
412 period band. Therefore, it could be considered that a large number of repeated
413 observations by altimeter satellites were executed during CSW events.

414 Fig. 8 shows a boxplot of along-track SLA over the continental shelf for tracks 12,
415 88, 114, and 190. The maxima, minima, and outliers derived from Fig. 8 are listed in
416 Table 2. The whisker dashed black line outside of the box extends to the most extreme
417 data points, not considering the outliers at the 5 % significance level. One can see that
418 the trapped characteristics as the maximum amplitude (75th percentile), interquartile
419 range (IQR), and outliers (red plus sign) occur at the coastal side. In contrast, the
420 minima occur at the edge of the continental shelf (150, 165, 105 and 165 km offshore
421 for tracks 12, 88, 114 and 190). The amplitude of along-track SLA for maxima and IQR
422 decreases gradually from the coastline (0.2-0.4 m) to the edge of the continental shelf
423 (~0.1). The largest outlier is 0.65 m over the shelf 30 km offshore.

424 The largest SLA over the shelf occur from July to September. For example, the
425 75th percentile of SLAs near the coastline is about 0.25 m for track 144, and 0.42 m for
426 track 88. The largest outlier of 0.65 m also occurs from July to September for track 88.
427 The smallest SLA occurs from April to June when the wind is weak during the monsoon
428 transition period (Wang et al., 2009). The extreme data from July to September show
429 the occurrences of storm surges over the shelf (Chen et al., 2014).

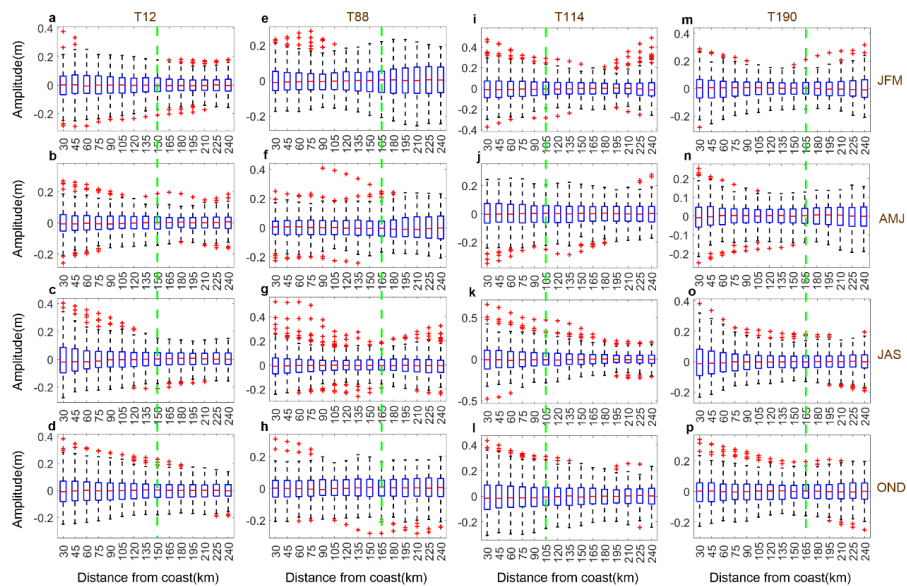
430 Overall, the maximum amplitude, IQR, and extreme data of the along-track data



431 over the shelf show the trapped wave characteristics, which shows that SLA decreases
432 gradually from the coastline to the edge of the continental shelf. The trapped
433 characteristics from the along-track SLA are similar to the cross-shelf structure of
434 normalized amplitudes of the mode 1 CSWs, as shown in Fig. 5a. It should contain
435 higher modes in the along-track SLA. The along-track SLA for tracks 153, 229 and 240
436 show similar characteristics (not perpendicular to the coastline, not shown).

437 Moreover, the theoretical CSW node is about 200 km (in track 12) offshore,
438 calculated by the given shelf breakpoint (Table 1). In contrast, the minimum STD (Fig.
439 3) and minimum distribution of along-track SLA (Fig. 8) are located at about 150 km
440 offshore, where the water depth is about 200 m. All the minimum STDs of along-track
441 SLA are found at the water depth of about 200 m. This indicates that the shelf break for
442 calculating theoretical CSWs should be set at the water depth of about 200-300 m, as
443 the node in Fig 5a would be closer to the coastline.

444



445

446 **Fig. 8.** Boxplot of along-track SLA over the shelf for tracks 12, 88, 114, and 190 from
447 1993 to 2020 (in the column). Seasonal means of SLA are plotted in the rows. Green
448 dashed lines present the minimum STD of the along-track SLA. The climatological
449 seasonal mean is removed. The along-track SLA is cut into small segments for every
450 15 km offshore, and averaged in each segment.



451

452 Table 2. Parameters extracted from along-track SLA in Fig. 8.

Track		T12 (150 km)				T88 (165 km)				T114 (105 km)				T190 (165 km)			
Position	(Distance)**	JFM	AMJ	JAS	OND	JFM	AMJ	JAS	OND	JFM	AMJ	JAS	OND	JFM	AMJ	JAS	OND
Coast	Outlier(m)	0.28	0.25	0.38	0.34	0.47	-0.35	0.65	0.43	0.23	0.24	0.52	0.31	0.38	0.27	0.41	0.38
	Maxi(m)	0.26	0.19	0.32	0.24	0.29	0.24	0.42	0.36	0.21	0.17	0.25	0.18	0.21	0.19	0.34	0.28
	Mini(m)	-0.23	-0.22	-0.24	-0.23	-0.3	-0.24	-0.33	-0.31	-0.17	-0.18	-0.24	-0.2	-0.25	-0.21	-0.28	-0.25
Edge	Outlier(m)	0.17	-0.15	0.19	0.19	0.23	-	0.29	-	0.21	0.39	0.28	0.16	-0.2	0.2	-0.2	0.21
	Maxi(m)	0.15	0.12	0.13	0.16	0.16	0.2	0.2	0.22	0.17	0.18	0.15	-0.18	0.16	0.12	0.14	0.17
	Mini(m)	-0.15	-0.14	-0.13	-0.15	-0.19	-0.2	-0.2	-0.21	-0.16	-0.14	-0.15	-0.2	-0.17	-0.13	-0.16	-0.17

453 *Coast is the position with the highest STD for each track, about 15 km offshore. Edge

454 is the position with the minimum STD of along-track SLA as shown in Fig. 8.

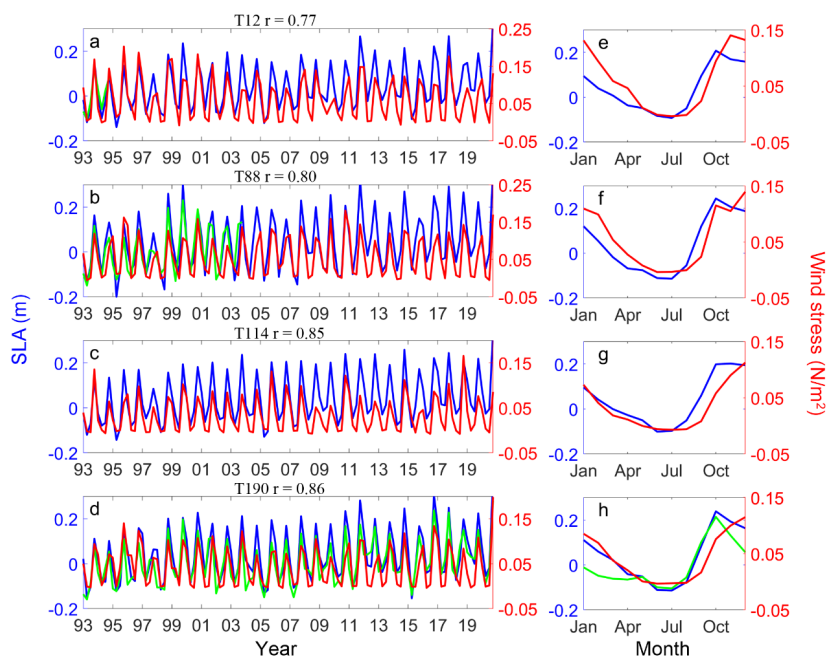
455 ** Distance between coastline and edge.

456

457 **2) ATWs**

458 As shown in Fig. 3, the inter-seasonal and seasonal signals could be distinguished
 459 from along-track SLA. Fig. 9 shows the seasonal mean of along-track SLA and along-
 460 shelf sea surface wind. One can see that the time series of the seasonal mean of along-
 461 track SLA show the seasonal variation with the amplitude of about 0.1-0.2 m at 15 km
 462 offshore. The time series of the seasonal mean of DSLA show similar characteristics
 463 with along-track SLA. The correlation relationship between the seasonal mean of
 464 along-track SLA and along-shelf sea surface winds reaches >0.77. The monthly mean
 465 of SLA during April-September is negative, while positive in the other months. It is
 466 attributed to that the local wind stress substantially influences the coastal sea level (Lin
 467 et al., 2022).

468



469

470

471

472

473

474

475

476

477

478

479

480

481

482

483

484

485

486

487

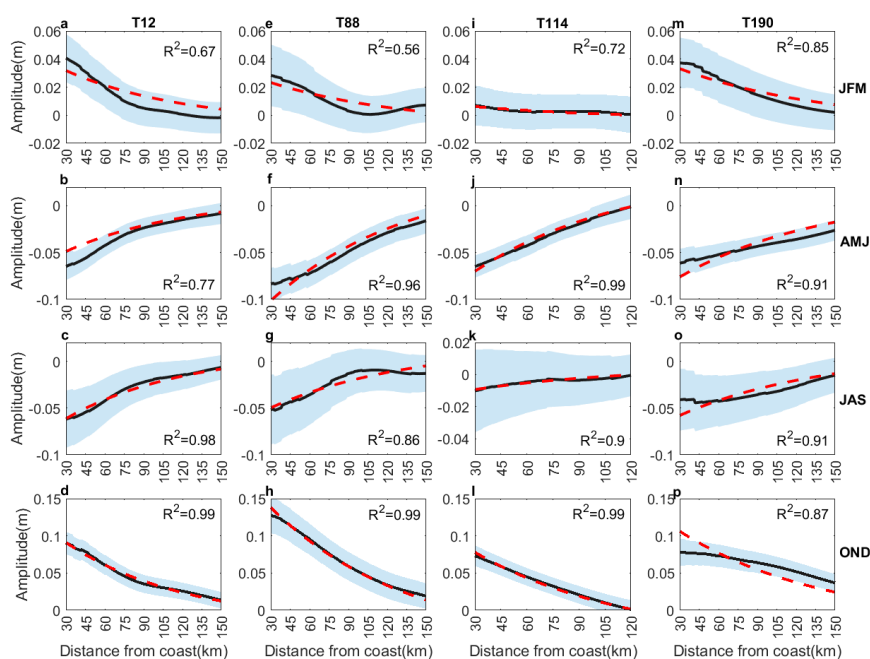
Fig. 9. Time series of the seasonal mean of along-track SLA and along-shelf sea surface wind stress for tracks (a)12, (b) 88, (c) 114, (d)190, and (e-h) monthly climatological mean of along-track SLA and along-shelf sea surface wind stress. Red curves represent the along-track SLA at 15 km offshore. Green curves represent the seasonal mean of sea level data at tide-gauge stations (a) Xiamen, (b) Shanwei, and (d) Zhapo.

Fig. 10 shows the cross structure of the seasonal mean of along-track SLA. One can see that the SLA on the coastline side is lower than on the ocean side from April to September. In the other seasons, the slope of along-track SLA is the opposite. The along-track SLA presents similar characteristics as shown in Fig. 9, i.e., the variation of SLA is controlled by the sea surface winds over the shelf.

Meanwhile, from Fig.10 one can see the cross-shelf structure of along-track SLA. The fitting curves show that theoretical ATWs (Fig. 6) explains the cross-shore structure of along-track SLA very well. The amplitudes of ATWs are 0.04 m, -0.06 m, -0.05 m, and 0.10 m in January-March, April-June, July-September, and October-December. Differently from Fig. 8, the amplitudes of ATWs during October-December are larger than that during July-September. It should be attributed to that the monsoon winds in winter are stronger than that in summer. Lin et al. (2021) investigated the tilt of mean



488 dynamic topography along the coast of the Chinese mainland. Their results confirm that
 489 the ATWs predict the coastal dynamic topography over the continental shelf of the SCS
 490 well.
 491



492 **Fig. 10.** Fitting climatologic seasonal mean of along-track SLA (black curves) using
 493 cross-shelf ATWs (red dashed curves) for tracks (a-d) 12, (e-h) 88, (i-l) 114, and (m-p)
 494 190. Dashed shadow is the STD of the seasonal mean of along-track SLA.
 495

496

497 6 Summary

498 Using sea level data derived from the tide-gauge stations Kanmen, Xiamen,
 499 Shanwei, Hongkong, and Zhapo, this study analyzes statistical features of the CSWs,
 500 inter-seasonal and seasonal signals. Meanwhile, along-track SLA data derived from
 501 multiple satellite altimeters from 1993 to 2020 are applied to detect the cross-shelf
 502 structures of the signals. The major results are summarized as follows.

- 503 1) The CSWs of periods shorter than 40 d propagate along the coast with the phase
 504 speed of about 10 m s⁻¹ in the ECS and 8 m s⁻¹ in the SCS. The dispersion relation
 505 of the waves indicates that the waves belong mode 1 CSWs.



506 2) Owing to the fact that the repeated observation period of the satellite altimeters is
507 comparable with that of CSWs, we combine fragments of the numerous repeated
508 observations of along-track SLA to reconstruct the cross-shelf structure of the
509 CSWs using 28 years of the abundant CSW data over the shelf. The results show
510 that the maximum amplitudes of CSWs have remarkable seasonal variability, about
511 0.6 m during July-September, while only 0.2 m during April-June. The
512 reconstructed cross-shelf structures of the CSWs confirm the property of mode 1
513 CSWs. Moreover, the energy is trapped within the partial continental shelf
514 shallower than 200 m.

515 3) The inter-seasonal and seasonal signals present as the ATWs over the continental
516 shelf. The amplitudes of ATWs have remarkable seasonal variability, ~ 0.10 m
517 during October-December, twice larger than 0.04 m, 0.05 m and -0.06 m during
518 January-March, July-September, and April-June, respectively. These results reveal
519 that the local wind stress substantially influences the ATWs over the continental
520 shelf.

521 4) The results derived from the observation data of along-coast tide-gauge stations
522 combined with cross-shelf tracks of satellite altimeters are interpreted well by the
523 framework of linear wave theory. It implies that the technological approaches
524 developed in this study are suitable for constructing the cross-shelf structures of
525 CSWs and ATWs over the continental shelf.

526

527 **Acknowledgments**

528 This research was funded by the National Key Research and Development Program of
529 China (2022YFC3104805); National Natural Science Foundation of China (42276019,
530 41476009, 41976200, 41506018, 41706025); Innovation Team Plan for Universities in
531 Guangdong Province (2019KCXTF021); and First-class Discipline Plan of Guangdong
532 Province (080503032101, 231420003).

533

534 **Data Availability Statement**

535 The tide gauge data are available at <https://psmsl.org/data/obtaining/>. The along-track



536 SLAs is obtained at <ftp-access.aviso.altimetry.fr>.

537

538 **Author contributions**

539 JYL were responsible for writing the original draft. Review and editing were conducted by QAZ.

540 Conceptualization was handled by JYL, QAZ and LLX. TH and YX were responsible for data

541 curation. LLX acquired funding.

542

543 **Competing interests**

544 The contact author has declared that none of the authors has any competing interests.

545

546 **Disclaimer**

547 Publisher's note: Copernicus Publications remains neutral with regard to jurisdictional claims in

548 published maps and institutional affiliations.

549

550 **References:**

551 Castro, B.M., Lee, T.N., 1995. Wind-forced sea level variability on the southeast Brazilian shelf. *Journal of*

552 *Geophysical Research: Oceans* 100, 16045-16056.

553 Chapman, D.C., 1987. Application of wind-forced, long, coastal-trapped wave theory along the California

554 coast. *Journal of Geophysical Research: Oceans* 92, 1798-1816.

555 Chen, D., Su, J., 1987. Continental shelf waves along the coasts of China. *Acta Ocean. Sin.* 3, 317-334.

556 Chen, N., Han, G., Yang, J., Chen, D., 2014. Hurricane Sandy storm surges observed by HY-2A satellite

557 altimetry and tide gauges. *Journal of Geophysical Research: Oceans* 119, 4542-4548.

558 Cheng, X., Qi, Y., 2007. Trends of sea level variations in the South China Sea from merged altimetry data.

559 *Global and Planetary Change* 57, 371-382.

560 Csanady, G.T., 1978. The Arrested Topographic Wave. *J. Phys. Oceanogr.* 8, 47-62.

561 Ding, Y., Bao, X., Shi, M., 2012. Characteristics of coastal trapped waves along the northern coast of the

562 South China Sea during year 1990. *Ocean Dyn.* 62, 1259-1285.

563 Ding, Y., Bao, X., Yao, Z., Song, D., Song, J., Gao, J., Li, J., 2018. Effect of coastal-trapped waves on the

564 synoptic variations of the Yellow Sea Warm Current during winter. *Cont. Shelf Res.* 167, 14-31.

565 Fang, G., Chen, H., Wei, Z., Wang, Y., Wang, X., Li, C., 2006. Trends and interannual variability of the



- 566 South China Sea surface winds, surface height, and surface temperature in the recent decade. *Journal of*
567 *Geophysical Research: Oceans* 111.
- 568 Gan, J., Li, H., Curchitser, E.N., Haidvogel, D.B., 2006. Modeling South China Sea circulation: Response
569 to seasonal forcing regimes. *Journal of Geophysical Research: Oceans* 111.
- 570 Ho, C.-R., Zheng, Q., Soong, Y.S., Kuo, N.-J., Hu, J.-H., 2000. Seasonal variability of sea surface height in
571 the South China Sea observed with TOPEX/Poseidon altimeter data. *Journal of Geophysical Research:*
572 *Oceans* 105, 13981-13990.
- 573 Hormazabal, S., Shaffer, G., Letelier, J., Ulloa, O., 2001. Local and remote forcing of sea surface
574 temperature in the coastal upwelling system off Chile. *Journal of Geophysical Research: Oceans* 106,
575 16657-16671.
- 576 Hsueh, Y., Pang, I.-C., 1989. Coastally Trapped Long Waves in the Yellow Sea. *J. Phys. Oceanogr.* 19, 612-
577 625.
- 578 Hsueh, Y., Romea, R.D., 1983. Wintertime winds and coastal sea-level fluctuations in the Northeast China
579 Sea. Part I: observations. *J. Phys. Oceanogr.* 13, 2091-2106.
- 580 Huang, D., Zeng, D., Ni, X., Zhang, T., Xuan, J., Zhou, F., Li, J., He, S., 2015. Alongshore and cross-shore
581 circulations and their response to winter monsoon in the western East China Sea. *Deep Sea Res. Part II.*
582 *Kajikawa, Y., Yasunari, T., 2005. Interannual variability of the 10–25- and 30–60-day variation over the*
583 *South China Sea during boreal summer. Geophysical Research Letters* 32.
- 584 Li, J., Zheng, Q., Hu, J., Fan, Z., Zhu, J., Chen, T., Zhu, B., Xu, Y., 2015. Wavelet analysis of coastal-
585 trapped waves along the China coast generated by winter storms in 2008. *Acta Ocean. Sin.* 34 22-31.
- 586 Li, J., Zheng, Q., Hu, J., Xie, L., Zhu, J., Fan, Z., 2016. A case study of winter storm-induced continental
587 shelf waves in the northern South China Sea in winter 2009. *Cont. Shelf Res.* 125, 127-135.
- 588 Li, J., Zheng, Q., Li, M., Li, Q., Xie, L., 2021. Spatiotemporal Distributions of Ocean Color Elements in
589 Response to Tropical Cyclone: A Case Study of Typhoon Mangkhut (2018) Past over the Northern South
590 China Sea. *Remote Sensing* 13, 687.
- 591 Li, L., 1993. A study of winter subtidal sea level fluctuation along the northern coast of the South China
592 Sea. *Tropic Oceanology.*
- 593 Lin, W., Lin, H., Hu, J., 2021. The Tilt of Mean Dynamic Topography and its Seasonality Along the Coast
594 of the Chinese Mainland. *Journal of Geophysical Research: Oceans* 126, e2020JC016778.
- 595 Lin, W., Lin, H., Hu, J., Huang, L., 2022. Relative Contributions of Open-Ocean Forcing and Local Wind



596 to Sea Level Variability Along the West Coasts of Ocean Basins. *Journal of Geophysical Research:*
597 *Oceans* 127, e2022JC019218.

598 Lin, X., Yang, J., 2011. An asymmetric upwind flow, Yellow Sea Warm Current: 2. Arrested topographic
599 waves in response to the northwesterly wind. *Journal of Geophysical Research: Oceans* 116.

600 Lin, X., Yang, J., Guo, J., Zhang, Z., Yin, Y., Song, X., Zhang, X., 2011. An asymmetric upwind flow,
601 Yellow Sea Warm Current: 1. New observations in the western Yellow Sea. *Journal of Geophysical*
602 *Research: Oceans* 116.

603 Marshall, A.G., Hendon, H.H., 2013. Impacts of the MJO in the Indian Ocean and on the Western Australian
604 coast. *Clim. Dyn.*, 1-17.

605 Rong, Z., Liu, Y., Zong, H., Cheng, Y., 2007. Interannual sea level variability in the South China Sea and
606 its response to ENSO. *Global and Planetary Change* 55, 257-272.

607 Schulz, W.J., Mied, R.P., Snow, C.M., 2011. Continental shelf wave propagation in the Mid-Atlantic Bight:
608 a general dispersion relation. *J. Phys. Oceanogr.* 42, 558-568.

609 Shen, J., Zhang, S., Zhang, J., Zeng, M., Fang, W., 2021. Observation of continental shelf wave propagating
610 along the eastern Taiwan Strait during Typhoon Meranti 2016. *Journal of Oceanology and Limnology*
611 39, 45-55.

612 Vialard, J., Shenoi, S., McCreary, J., Shankar, D., Durand, F., Fernando, V., Shetye, S., 2009. Intraseasonal
613 response of the northern Indian Ocean coastal waveguide to the Madden-Julian Oscillation. *Geophys.*
614 *Res. Lett.* 36.

615 Wang, B., Huang, F., Wu, Z., Yang, J., Fu, X., Kikuchi, K., 2009. Multi-scale climate variability of the
616 South China Sea monsoon: A review. *Dyn. Atmos. Oceans* 47, 15-37.

617 Wang, H., Li, W., Xiang, W., 2022. Sea level rise along China coast in the last 60 years. *Acta Oceanologica*
618 *Sinica* 41, 18-26.

619 Wang, H., Liu, K., Gao, Z., Fan, W., Liu, S., Li, J., 2017. Characteristics and possible causes of the seasonal
620 sea level anomaly along the South China Sea coast. *Acta Oceanologica Sinica* 36, 9-16.

621 Xie, L., Zheng, Q., Zhang, S., Hu, J., Li, M., Li, J., Xu, Y., 2018. The Rossby normal modes in the South
622 China Sea deep basin evidenced by satellite altimetry. *International Journal of Remote Sensing* 39, 399-
623 417.

624 Xu, Y., Lin, M., Zheng, Q.a., Song, Q., Ye, X., 2016. A study of sea level variability and its long-term trend
625 in the South China Sea. *Acta Oceanologica Sinica* 35, 22-33.



- 626 Yin, L., Qiao, F., Zheng, Q., 2014. Coastal-trapped waves in the East China Sea observed by a mooring
627 array in winter 2006. *J. Phys. Oceanogr.* 44, 576-590.
- 628 Zhao, R., Zhu, X.-H., Park, J.-H., 2017. Near 5-Day Nonisostatic Response to Atmospheric Surface
629 Pressure and Coastal-Trapped Waves Observed in the Northern South China Sea. *J. Phys. Oceanogr.* 47,
630 2291-2303.
- 631 Zheng, Q., And, G.F., Song, Y.T., 2006. Introduction to special section: Dynamics and Circulation of the
632 Yellow, East, and South China Seas. *Journal of Geophysical Research: Oceans*.
- 633 Zheng, Q., Hu, J., Zhu, B., Feng, Y., Jo, Y.-H., Sun, Z., Zhu, J., Lin, H., Li, J., Xu, Y., 2014. Standing wave
634 modes observed in the South China Sea deep basin. *Journal of Geophysical Research: Oceans* 119, 4185-
635 4199.
- 636 Zheng, Q., Zhu, B., Li, J., Sun, Z., Xu, Y., Hu, J., 2015. Growth and dissipation of typhoon-forced solitary
637 continental shelf waves in the northern South China Sea. *Clim. Dyn.* 45, 853-865.
- 638 Zhuang, W., Xie, S.P., Wang, D.X., Taguchi, B., Aiki, H., Sasaki, H., 2010. Intraseasonal variability in sea
639 surface height over the South China Sea. *Journal of Geophysical Research-Oceans* 115.
- 640
- 641